GROWTH AND CHARACTERIZATION OF RUBIDIUM COPPER SULFIDE

AN HONORS THESIS
SUBMITTED TO THE DEPARTMENT OF PHYSICS
AND THE COMMITTEE ON UNDERGRADUATE STUDIES
OF STANFORD UNIVERSITY
IN PARTIAL FULFILLMENT OF THE REQUIREMENTS
FOR THE DEGREE OF
BACHELOR OF SCIENCE WITH HONORS

Maxwell C. Shapiro
May 2010

I certify that I have read this thesis and that, in my opinion, it is fully adequate in scope and quality as a thesis for the degree of Bachelor of Science with Honors.

(Ian R. Fisher) Principal Advisor

I certify that I have read this thesis and that, in my opinion, it is fully adequate in scope and quality as a thesis for the degree of Bachelor of Science with Honors.

(Theodore H. Geballe)

Approved for the University Committee on Undergraduate Studies.

Abstract

In this thesis I describe the synthesis and physical properties of a novel ternary compound $RbCu_4S_3$. The material is a bilayer variant of the familiar $ThCr_2Si_2$ structure (adopted, for instance, by several members of the iron-pnictide family of superconductors, including $BaFe_2As_2$ [1]). Interest in this quasi-low-dimensional compound revolves around its potential to harbor an electronic instability, for example a charge density wave. After establishing a suitable procedure to grow high quality single crystals, my ongoing experiments have probed the nature of the $RbCu_4S_3$ ground state via a combination of transport and thermodynamic measurements. The results of these experiments have been compared with band structure calculations performed using the WIEN2K software package. Additional x-ray diffraction and transmission electron microscopy (TEM) structural characterization has been performed by collaborators.

The calculated Fermi surface of $RbCu_4S_3$ reveals one three-dimensional pocket and two quasi-two-dimensional pockets with considerable potential for nesting. However, neither single crystal x-ray diffraction refinements nor high resolution TEM measurements indicate the presence of a lattice modulation in this material. The electrical resistivity is that of a good metal, with a very low residual resistivity and a correspondingly high residual resistance ratio ($RRR_{typical} = \frac{\rho(300K)}{\rho_0} \geq 600$). Such high quality samples permit the observation of quantum oscillatory effects in high magnetic fields, providing a direct probe of the Fermi surface morphology and the quasiparticle effective mass. Preliminary measurements of Shubnikov-de Haas oscillations in the magnetoresistance for fields oriented along the crystalline c-axis reveal several frequencies corresponding to different extremal orbits of the various Fermi

surface pockets. Comparison with the calculated band structure leads to a tentative assignment for at least one of these orbits with the three-dimensional hole pocket, but additional angle-dependent measurements will be necessary to make an unambiguous comparison. Heat capacity measurements yield a Sommerfeld coefficient $\gamma = 13.1 \pm .04$ mJ/mol K^2, which is larger by a factor of ~ 1.6 over that estimated from our band structure calculations, presumably reflecting mass renormalization due to many-body effects. Taken together, the preponderance of the evidence suggests that $RbCu_4S_3$ does not suffer an electronic instability, although further experiments will be necessary to conclusively establish whether or not this is the case.

Acknowledgements

First and foremost, I would like to thank my advisor, Ian Fisher, for giving me the wonderful opportunity of conducting research in his laboratory as an undergraduate. I greatly appreciate the patience and generosity that Ian has shown me, and his enthusiasm for scientific discovery is completely contagious.

To all of my labmates in the Fisher Lab, thank you all for your support and help. It has been very enjoyable for me to assist Eric as he works toward completing his Ph.D. Eric has pretty much taught me everything I know about experimental science in the lab, and he has been a wonderful mentor and friend. Many thanks to Jim for answering all of my incessant questions, for helping me run the WIEN2k software, and for being a stand-up guy. Your quirky sense of humor rubbed off on me as I hope mine has on you. Thank you to Felipe and Hsueh-Hui for teaching me how to do contacts and for always being there for a friendly chat. Thank you to Jiun-Haw for being willing to help out a lowly undergraduate who is unsure of how to use a machine. Every time I have talked to you, I feel that I have learned something new that makes me think of things in a slightly different way. To all of you—and to Chris and Paula too—thanks for making the Fisher Lab an awesome place to do science.

I would like to thank our collaborators for their contributions to the project as well. Thank you to Professor Julia Chan and her student Adam Phelan for their single crystal x-ray diffraction measurements. Thanks to Professor Matthew Kramer for his help in performing TEM measurements looking for superlattice modulations. Thank you to Patrick Kirchmann and Jonathan Sobota for their efforts in performing ARPES.

Finally, I would like to thank my parents for all of their support.

Contents

Abstract **iii**

Acknowledgements **v**

1 Introduction **1**

1.1 Instabilities in Low-Dimensional Materials 1

1.2 $RbCu_4S_3$ 2

1.3 Outline 4

2 Theory **5**

2.1 The Onsager Relation 5

2.2 Shubnikov-de Haas Effect 7

2.3 The Debye Model 8

2.4 Free Electron Gas 10

3 Experimental Methods **12**

3.1 Crystal Growth & Characterization 12

3.2 Transport Measurements 14

3.3 Heat Capacity Measurements 15

4 Results **16**

4.1 Resistivity Results 16

4.2 Shubnikov-de Haas Results 17

4.3 Heat Capacity Results 20

5 Discussion **22**

5.1 Electronic Band Structure Calculations for $RbCu_4S_3$ 22

5.2 Comparison with Results 25

6 Conclusion **26**

Bibliography **27**

Chapter 1

Introduction

1.1 Instabilities in Low-Dimensional Materials

Charge density waves (CDWs) involve the periodic distortion of the charge carrier density in a material. These ordered states are frequently associated with low-dimensional, anistropic materials [2]. One mechanism that can drive CDW formation is Fermi surface nesting. Nesting wave vectors redistribute charge in such a way that they introduce a new spatial periodicity, not necessarily coincident with that of the lattice. This redistribution creates energy gaps at the Fermi level which lower the total energy of the system.

CDWs, and also the closely related case of spin density waves (SDWs), are of interest physically in themselves, but the presence of these instabilities sometimes signal the potential for superconductivity. Two examples of this that have been studied extensively in our group are the rare-earth tritellurides $R\mathrm{Te}_3$ (CDW) [3] and $\mathrm{BaFe}_2\mathrm{As}_2$ (SDW) [4], whose phase diagrams are reproduced in Figures 1.1 and 1.2. In both instances, the ground state can be tuned by an external parameter, providing the driving force for the phase transition.

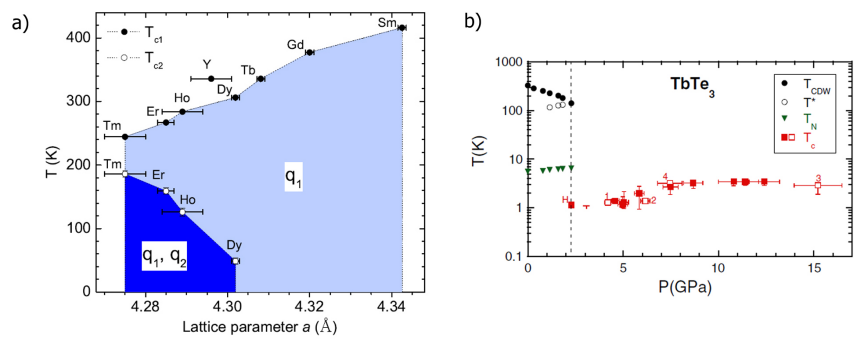

Figure 1.1: a) Phase diagram taken from [3] for the rare-earth tritellurides. Below T_{c1}, a CDW forms with wavevector q_1. Below T_{c2}, an additional CDW forms with wavevector q_2. b) Taken from [5]. Suppressing the CDW by applying pressure leads to a superconducting ordered state.

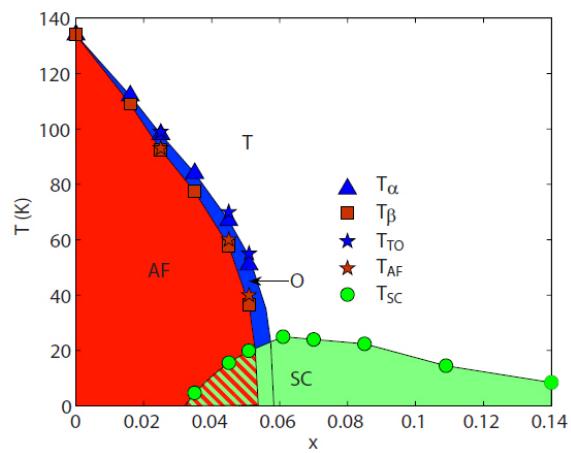

Figure 1.2: Phase diagram taken from [4] for $Ba(Fe_{1-x}Co_x)_2As_2$. Depending on the doping concentration of cobalt, different ordered states with different structure types obtain. Superconductivity arises from the suppression of the SDW. In the figure, AF refers to an anti-ferromagnetic ordered state, SC to a superconducting one, T for the tetragonal structure type, and O for orthorhombic.

1.2 $RbCu_4S_3$

$RbCu_4S_3$ is a member of a family of layered monovalent metal-copper chalcogenides including $TlCu_4S_3$ [6], $TlCu_4Se_3$ [7], KCu_4S_3 [8], KCu_4Se_3 [9], $RbCu_4Se_3$ [9], $CsCu_4S_3$

[10], and $CsCu_4Se_3$ [11]. The structure consists of double layers of copper ions which are tetrahedrally coordinated by sulfur atoms. These double layers are separated by rubidium ions, as depicted in Figure 1.3.

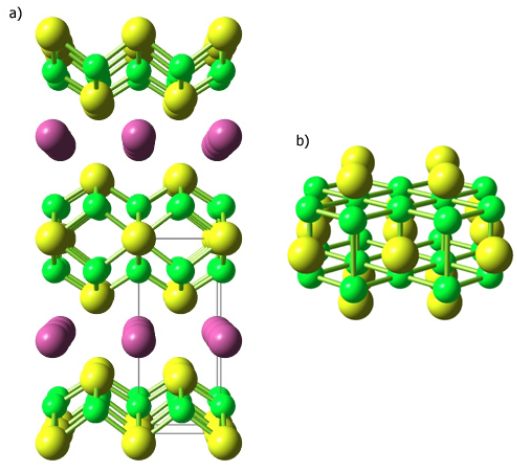

Figure 1.3: The crystal structure of $RbCu_4S_3$, a tetragonal system in the space group $P4/mmm$ with lattice parameters $a = b = 3.9288$ Å and $c = 9.431$ Å [12]. It can be considered a bilayer variant of the $ThCr_2Si_2$ structure. a) The colored spheres represent the following atoms: purple - rubidium, green - copper, yellow - sulfur. b) The principal structural motif is that of a double layer of copper ions arranged on a square lattice. The copper ions are tetrahedrally coordinated by sulfur. Lines are drawn between nearest neighbor copper ions to illustrate the arrangement of the cations.

We were initially drawn to $RbCu_4S_3$ because its empirical formulation suggests a formal mixed-valence Cu(I,II) system [13]. Since all of the copper ions are crystallographically equivalent, this makes $RbCu_4S_3$ a candidate material for realizing Jahn-Teller lattice distortions which can lead to enhanced electron-phonon coupling. However, early photoelectron spectroscopy indicates a single copper valence and the formation of broad, partially-filled sulfur valence bands [6]. Our own band structure calculations (described in more detail in Chapter 5) indicate a quasi low-dimensional electronic structure, exhibiting considerable potential for nesting. Given the general interest in quasi-low-dimensional materials, it is therefore of interest to establish the

nature of the ground state of $RbCu_4S_3$. We chose this specific member of this family of compounds principally because we were able to grow relatively large high quality single crystals, enabling a series of experiments probing the thermodynamic and transport properties.

1.3 Outline

In this thesis I describe the ongoing experiments designed to address the nature of the $RbCu_4S_3$ ground state. Chapter 2 is devoted to the background theory that describes magnetic oscillations in solids and low temperature heat capacity. Chapter 3 concerns crystal synthesis procedures and experimental methods. Chapter 4 presents results of transport and heat capacity measurements, including the observation of quantum oscillations. Finally, Chapter 5 discusses the experimental data in light of theoretical electronic band structure calculations.

Chapter 2

Theory

2.1 The Onsager Relation

The treatment presented here is taken from [14].

The essential cause of the Shubnikov-de Haas (SdH) effect (oscillations in resistance as a function of magnetic field) is the quantization of electron motion, which imposes a restriction on the permissible electron states. The Bohr-Sommerfeld quantization condition governs this restriction:

$$\oint \mathbf{p} \cdot d\mathbf{q} = (r + \gamma) 2\pi\hbar, \tag{2.1}$$

where $\mathbf{p}$ and $\mathbf{q}$ are conjugate momentum and position variables, r is an integer, γ is a phase constant which we set to $\frac{1}{2}$ (strictly, this is only exact for a parabolic band, but this will be unimportant for our discussion), and the integral is taken around a complete orbit. For an electron in a magnetic field $\mathbf{H}$, the conjugate variables are given by

$$\mathbf{p} = \hbar\mathbf{k} - e\mathbf{A}/c \tag{2.2}$$

$$\mathbf{q} = \mathbf{R'}, \tag{2.3}$$

where $\mathbf{k}$ is the wavevector of the electron, $-e$ is the electron charge, $\mathbf{A}$ is the vector

potential of $\mathbf{H}$ given by $\mathbf{H} = \nabla \times \mathbf{A}$, and $\mathbf{R'}$ is the projection of the real space trajectory onto a plane normal to $\mathbf{H}$.

In the presence of the magnetic field, the electron experiences a Lorentz force that changes its momentum according to

$$\hbar\dot{\mathbf{k}} = \frac{-e}{c}(\mathbf{v} \times \mathbf{H}), \tag{2.4}$$

which upon integrating with respect to time implies

$$\hbar(\mathbf{k} - \mathbf{k}_0) = \frac{-e}{c}(\mathbf{R} - \mathbf{R}_0) \times \mathbf{H}. \tag{2.5}$$

Here, $\mathbf{R}$ is the real space trajectory of the electron and $\mathbf{R}_0$ and $\mathbf{k}_0$ are reference vectors in real and reciprocal space (respectively). Plugging in (2.5) into (2.1) and noting that the reference vectors contribute nothing to the integral, one obtains

$$(r + \frac{1}{2})2\pi\hbar = \left(\frac{e}{c}\right)(\mathbf{H} \cdot \oint \mathbf{R} \times d\mathbf{R'} - \oint \mathbf{A} \cdot d\mathbf{R'}). \tag{2.6}$$

By employing Stokes' Theorem to the second integral and breaking up $\mathbf{R}$ into a component normal to $\mathbf{H}$ ($\mathbf{R'}$) and a component along $\mathbf{H}$ ($\mathbf{R_H}$), (2.6) yields

$$H\alpha = (r + \frac{1}{2})\frac{2\pi\hbar c}{e}, \tag{2.7}$$

where α is the area of the $\mathbf{R'}$ orbit in real space, given by $\alpha = \frac{1}{2} \parallel \oint \mathbf{R'} \times d\mathbf{R'} \parallel = \int_{\mathbf{S}} d\mathbf{S}$. Multiplying α by the area conversion factor $\left(\frac{c\hbar}{eH}\right)^2$ between real and reciprocal space, we finally arrive at the Onsager relation

$$a(\epsilon, \kappa) = (r + \frac{1}{2})\frac{2\pi eH}{c\hbar}, \tag{2.8}$$

where a is the area of the orbit in reciprocal space. In (2.8), the dependence of the area on the energy ϵ of the chosen constant energy surface and upon the magnitude of the chosen wavevector κ has been emphasized.

The geometrical interpretation of (2.8) is that the allowed electronic states in the presence of a magnetic field are restricted to tubes in k-space (so-called Laundau

tubes). As the magnetic field increases, individual tubes cross the Fermi surface one-by-one. The occupied lengths of the tubes shrink with this increase in field and vanish infinitely rapidly when the cross-sectional area $a(\epsilon, \kappa)$ equals the extremal area A of the Fermi surface. These vanishings occur at equal intervals of inverse field

$$\Delta(\frac{1}{H}) = \frac{2\pi e}{\hbar c A}, \tag{2.9}$$

and hence with a frequency

$$f \equiv \frac{1}{\Delta(\frac{1}{H})} = \frac{c\hbar A}{2\pi e}. \tag{2.10}$$

2.2 Shubnikov-de Haas Effect

This treatment is also taken from [14].

The SdH effect occurs because of oscillations in the density of states of the electrons. In order to see this oscillatory behavior, we first note that the differential contribution to the density of states from a two-dimensional slice of k-space with thickness dκ is

$$\delta\mathcal{D}(\epsilon) = D \sum_{r=0}^{\infty} \left(\frac{da}{d\epsilon}\right)_{\kappa} \delta\left[a(\epsilon, \kappa) - \left(r + \frac{1}{2}\right)\frac{2\pi e H}{\hbar c}\right], \tag{2.11}$$

where D is a degeneracy factor given by $D = \frac{eHVd\kappa}{2\pi^2\hbar c}$ (V is the real space volume of the metal) and $\left(\frac{da}{d\epsilon}\right)_{\kappa}$ is needed to normalize the δ-function. The form (2.11) makes sense since the only terms which contribute to the sum are those where the argument of the δ-function is zero (i.e., where a is an extremal area, as presented in the previous section).

If we now take as a definition of the effective mass $m(\epsilon) \equiv \frac{\hbar^2}{2\pi}\left(\frac{\partial a}{\partial \epsilon}\right)_{\kappa}$ and define a dimensionless variable $x \equiv \frac{\hbar c a(\epsilon,\kappa)}{2\pi e H}$, we can rewrite (2.11) as

$$\delta\mathcal{D}(\epsilon) = \frac{m(\epsilon)Vd\kappa}{2\pi^2\hbar^2} \sum_{r=0}^{\infty} \delta\left[x - \left(r + \frac{1}{2}\right)\right], \tag{2.12}$$

the Fourier transform of which is

$$\delta\mathcal{D}(\epsilon) = \frac{m(\epsilon)V d\kappa}{2\pi^2\hbar^2}\left[1 + 2\sum_{p=1}^{\infty}\cos\left(2\pi p\left(x - \frac{1}{2}\right)\right)\right]. \tag{2.13}$$

Evaluating (2.13) at the Fermi energy $\epsilon = \zeta$, we see that $\delta(\zeta)$ is composed of one oscillating and one non-oscillating component. Since the density of states is proportional to the number of carriers which is inversely proportional to the resistance, oscillations in the density of states are reflected as oscillations in the resistance.

At absolute zero temperature, we expect the amplitude of the oscillations to all be of the same magnitude. However, the effect of finite temperature is a sort of "phase smearing" in which the single, well-defined frequency f (which enters into (2.12) through $x(\zeta) = f/H$) is broadened over a small range of frequencies centered around f. This reduces the amplitudes of the oscillations by the reduction factor

$$R_T = \frac{\frac{2\pi^2 p k_B T}{\beta H}}{\sinh\left(\frac{2\pi^2 p k_B T}{\beta H}\right)}, \tag{2.14}$$

where p refers to the particular harmonic, k_B is the Boltzmann constant, and $\beta \equiv \frac{e\hbar}{mc}$ (m is the effective carrier mass).

2.3 The Debye Model

The treatment given here is largely taken from [15] and [16].

For the low-temperature dependence of the heat capacity, we treat the phononic and electronic contributions separately. Adding the two together provides the correct empirical form to fit to experiment. In what follows, we model the phononic contribution by way of the Debye model and the electronic contribution by way of the free electron gas model, proceeding with the phonons first.

In the Debye approximation scheme, we take the phonons to obey a linear dispersion

$$\omega = c_s k, \tag{2.15}$$

where c_s is the constant speed of sound of the phonons in the metal. In three dimensions (3D), this corresponds to a density of states of

$$D(\omega) = \frac{\omega^2 V}{2\pi^2 c_s^3}, \tag{2.16}$$

where V is the real space volume. The expression (2.16) is valid only up until some cutoff frequency ω_D, beyond which no modes are allowed. Since phonons are bosons, in thermal equilibrium their occupation numbers obey the Planck distribution:

$$\langle n \rangle = \frac{1}{e^{\frac{\hbar\omega}{k_B T}} - 1}. \tag{2.17}$$

By taking a weighted average of the phonon energy $\hbar\omega$ and integrating over all frequencies, we can obtain the total phononic contribution to the thermal energy U_p:

$$\begin{aligned} U_p &= 3\int_0^{\omega_D} d\omega D(\omega)\langle n\rangle \hbar\omega = 3\int_0^{\omega_D} d\omega \left(\frac{\omega^2 V}{2\pi^2 c_s^3}\right) \frac{\hbar\omega}{e^{\frac{\hbar\omega}{k_B T}} - 1} \\ &= \left(\frac{3Vk_B^4 T^4}{2\pi^2 c_s^3 \hbar^3}\right) \int_0^{x_D} dx \left(\frac{x^3}{e^x - 1}\right), \end{aligned} \tag{2.18}$$

where the extra factor of 3 comes from the different polarization directions in 3D, the variable substitution $x \equiv \frac{\hbar\omega}{k_B T}$ has been made, and we have defined $x_D \equiv \frac{\hbar\omega_D}{k_B T}$.

In the low temperature limit, $\lim_{T\to 0} x_D = \infty$, and hence

$$\begin{aligned} \lim_{T\to 0} U_p &= \left(\frac{3Vk_B^4 T^4}{2\pi^2 c_s^3 \hbar^3}\right) \int_0^{\infty} dx \left(\frac{x^3}{e^x - 1}\right) \\ &= \left(\frac{3Vk_B^4 T^4}{2\pi^2 c_s^3 \hbar^3}\right) \left(\frac{\pi^4}{15}\right) = \left(\frac{\pi^2 V k_B^4 T^4}{10 c_s^3 \hbar^3}\right). \end{aligned} \tag{2.19}$$

Since the phononic contribution to the heat capacity is $C_V = \frac{dU_p}{dT}$, we immediately see that

$$\lim_{T\to 0} C_V = \left(\frac{2V\pi^2 k_B^4 T^3}{5 c_s^3 \hbar^3}\right) \tag{2.20}$$

gives the characteristic low temperature dependence due to phonons.

2.4 Free Electron Gas

We now examine the case of the free electron gas, following [15] and [16].

The probability that a state at energy ϵ will be occupied in an ideal electron gas at thermal equilibrium is given by the Fermi-Dirac distribution:

$$f(\epsilon) = \frac{1}{e^{\frac{\epsilon-\mu}{k_B T}} + 1}, \tag{2.21}$$

where μ is the chemical potential, which at absolute zero temperature is equal to the Fermi energy ϵ_F. In general, the chemical potential is a function of the temperature.

One of the important features of (2.21) is that it has a characteristic width of order $k_B T$. Thus, at low temperatures (that is, for temperatures such that $T \ll \frac{\epsilon_F}{k_B}$), the function is essentially a step function, equal to 1 for $\epsilon < \mu$ and equal to 0 for $\epsilon > \mu$. This implies that the temperature derivative $\frac{df(\epsilon)}{dT}$ is strongly peaked at $\epsilon = \mu \approx \epsilon_F$ for low temperatures. This property will be used in what follows.

The increase in total energy in heating a system of N electrons to a temperature T from absolute zero is given by

$$U_{el} = \int_0^\infty \epsilon D(\epsilon) f(\epsilon) d\epsilon - \int_0^{\epsilon_F} \epsilon D(\epsilon) d\epsilon, \tag{2.22}$$

where $D(\epsilon)$ is the density of states. Using the identities $N = \int_0^\infty D(\epsilon) f(\epsilon) d\epsilon = \int_0^{\epsilon_F} D(\epsilon) d\epsilon$ and $\left(\int_0^{\epsilon_F} + \int_{\epsilon_F}^\infty\right) \epsilon_F f(\epsilon) D(\epsilon) d\epsilon = \int_0^{\epsilon_F} \epsilon_F D(\epsilon) d\epsilon$, (2.22) can be rearranged as

$$U_{el} = \int_{\epsilon_F}^\infty (\epsilon - \epsilon_F) f(\epsilon) D(\epsilon) d\epsilon + \int_0^{\epsilon_F} (\epsilon_F - \epsilon)(1 - f(\epsilon)) D(\epsilon) d\epsilon. \tag{2.23}$$

The intuition behind (2.23) is that the first term expresses the required energy for elevating electrons in levels of energy $\epsilon = \epsilon_F$ to higher energy levels and the second gives the required energy for elevating electrons up to an energy ϵ_F from lower energy

levels. From (2.23), we compute the heat capacity by taking a derivative with respect to temperature and noting that $f(\epsilon)$ is the only temperature dependent term:

$$C_{el} = \frac{dU_{el}}{dT} = \int_0^\infty (\epsilon - \epsilon_F)\frac{df(\epsilon)}{dT}D(\epsilon)d\epsilon \cong D(\epsilon_F)\int_0^\infty (\epsilon - \epsilon_F)\frac{df(\epsilon)}{dT}d\epsilon. \tag{2.24}$$

where in the last step we have used the fact that $\frac{df(\epsilon)}{dT}$ is a sharply peaked function at $\epsilon = \epsilon_F$ for low temperatures, as discussed above.

Since $f(\epsilon)$ is given explicitly by (2.21), we can compute its derivative to rewrite (2.24). Plugging this in, using that $\mu \approx \epsilon_F$ for low temperatures, and making the variable substitution $x \equiv \frac{\epsilon - \epsilon_F}{k_B T}$, we obtain that

$$C_{el} = k_B^2 T D(\epsilon_F)\int_{-\frac{\epsilon_F}{k_B T}}^\infty \frac{x^2 e^x}{(e^x+1)^2}dx. \tag{2.25}$$

For the low temperature limit we are considering, $\frac{\epsilon_F}{k_B T} \to -\infty$, and hence the integral expression can be evaluated explicitly. The result is $\frac{\pi^2}{3}$, giving the form of the electronic contribution to the heat capacity as

$$C_{el} = \frac{1}{3}\pi^2 k_B^2 D(\epsilon_F)T, \tag{2.26}$$

which is directly proportional to the density of states at the Fermi level and linear in temperature.

By superposing the electronic and phononic contributions, we see that the general form for the heat capacity at low temperatures is

$$C = \gamma T + AT^3, \tag{2.27}$$

where γ is a fit parameter proportional to $D(\epsilon_F)$.

Chapter 3

Experimental Methods

3.1 Crystal Growth & Characterization

Initial attempts at growing single $RbCu_4S_3$ crystals were based on the work done by Rudorff *et. al.* [12]. The recipe there calls for a mixture of rubidium sulfide, copper, and sulfur in the molar ratio 1 Rb_2S : 4 Cu : 2.7 S peformed in a sealed, evacuated quartz tube and up to a temperature of between 800 and 850 C. As rubidium sulfide is not readily available commercially in the United States and its synthesis requires handling elemental rubidium, which can be highly hazardous due to its high reactivity, the growth technique used here instead uses rubidium carbonate (Rb_2CO_3).

Because the Rb_2CO_3 releases CO_2 during the course of the reaction, the growth could not be sealed without a heightened probability of explosion due to overpressure. Instead, crystals were grown by placing the precursor materials in a 2 mL alumina crucible and capped by a larger 5 mL alumina crucible. Capping the 2 mL crucible was crucial for crystal formation, as otherwise evaporation caused a significant sulfur deficiency in the melt. The growth itself was performed in a horizontal tube furnace with flowing argon.

After systematic iteration about the procedure given in [12], the optimized molar ratios were 1 Rb_2CO_3 : 4.42 Cu : 5.17 S. The optimal temperature cycle was a rapid ramp up to 800 C in 2 hours and then a fast furnace cool to room temperature. The crystals were mechanically extracted from the bulk. Crystal size varied but generally

fell in the 500 μm – 1 mm range in either dimension.

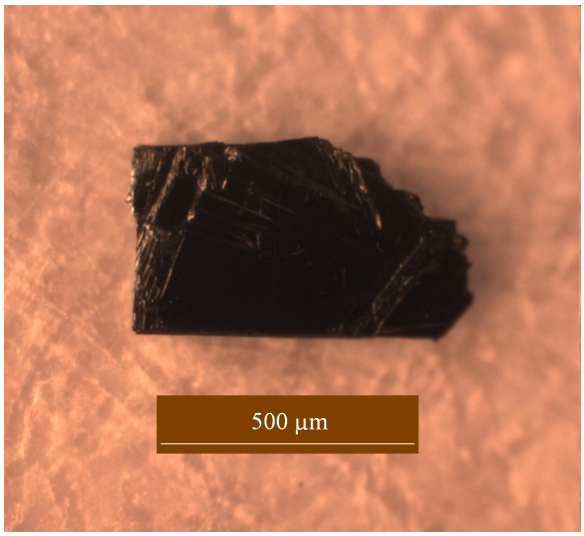

Figure 3.1: Photograph of a typical crystal of $RbCu_4S_3$. The crystals have a plate-like morphology, with the long c-axis perpendicular to the plane of the plates.

A typical crystal is shown in Figure 3.1. The crystals themselves were mostly flat, save for at the edges, which are indicative of minimal crystal intergrowth. The crystals are black in color, possibly indicating a low plasma frequency and motivating further exploration into the nature of the ground state. The crystals did not appear to be especially air-sensitive, although cleaning in isopropanol, methanol, or water significantly deterioriated the crystal sheen.

A single predominant phase was confirmed by x-ray diffraction measurements. Powder x-ray diffraction patterns were obtained by grinding a large number of single crystals embedded in a matrix of solidified flux. Comparison with published data demonstrated that the predominant phase was $RbCu_4S_3$. Single crystal x-ray diffraction experiments performed by Professor Julia Chan and Adam Phelan at Louisiana State University confirmed that the crystals are indeed $RbCu_4S_3$. Parameters of the structural refinement all agreed with published data [6].

Additional structural characterization was provided by high resolution TEM in collaboration with Professor Matthew Kramer at the Ames Laboratory at Iowa State

University. These measurements did not reveal any indication of a superlattice modulation.

3.2 Transport Measurements

Resistance data were obtained via a standard four-point probe measurement technique. 12.5 μm gold wire contacts were attached by using EPO-TEK H20E silver epoxy and then curing the samples at 150 C. In order to decrease contact resistance, gold pads were deposited with the aid of a Cressington 108 Sputter Coater. Without gold deposition, contact resistances were too high to obtain reliable data. A typical arrangement is shown in Figure 3.2.

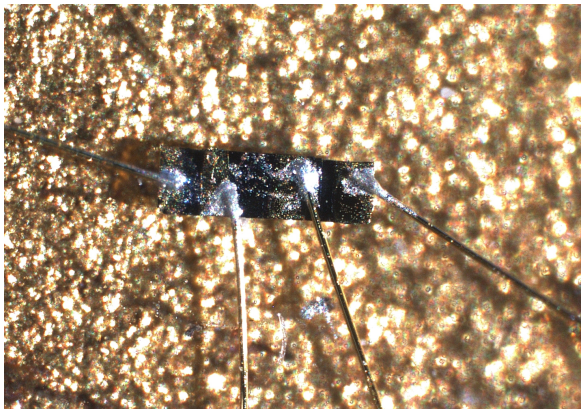

Figure 3.2: Electrical contacts on a sample. The crystal shown is approximately 680 μm in length. The sample has been cleaved into a rod-like shape to provide a better estimate of the resistivity. In addition, the low resistivity of the material due to the high crystal quality requires relatively narrow samples in order to measure the resistance at low temperature.

Measurements were performed in a commercial Quantum Design physical properties measurement system (PPMS). The PPMS uses a liquid helium-cooled superconducting magnet to generate magnetic fields up to 14 T at temperatures down to 1.8 K.

3.3 Heat Capacity Measurements

Heat capacity data were obtained by employing a two-τ thermal relaxation time technique. First, samples were mounted on a platform with grease, both of which are in thermal contact with a heater. The heater raises the temperature of the platform-sample system until it exponentially settles at some higher temperature and then abruptly shuts off. By measuring the platform-sample temperature before heating, after equilibrating at the higher temperature, and after the heater has turned off, the heat capacity can be extracted from the slopes of the heating and cooling curves and the power rating of the heater.

In order to measure a reliably high signal, 12 crystals of total mass .98 ± .01 mg were used. This completely covered the sample platform, as shown in Figure 3.3. An addenda measurement was performed to subtract out the background signal due to the presence of the grease and platform.

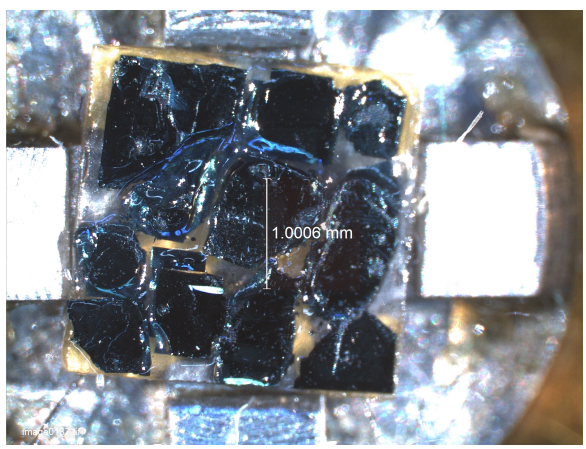

Figure 3.3: Samples mounted on a platform for a heat capacity measurement.

As with the transport measurements, the heat capacity measurements were performed in a PPMS. Liquid helium-3 was used to get to temperatures as low as 370 mK.

Chapter 4

Results

4.1 Resistivity Results

A sample resistivity versus temperature measurement in zero magnetic field is plotted in Figure 4.1.

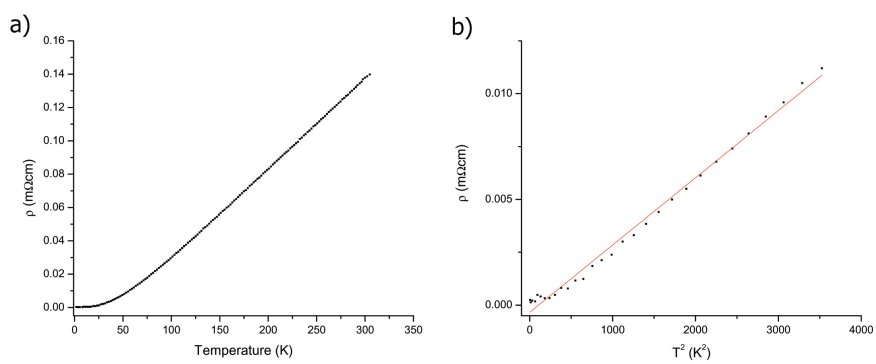

Figure 4.1: Resistivity versus temperature at zero field. a) The curve is linear for most of the temperature range until it levels off at low temperatures at a value $\rho_0 = 1.5 \times 10^{-4}$ mΩcm. The RRR value for the crystal shown (which is the same crystal as used for the SdH measurements shown in the next section) is 902. b) For temperatures below 60 K, the resistivity rises quadratically with temperature (linear fit shown in red). This is a characteristic signature of electron-electron scattering in a good metal.

The general form of Figure 4.1 remains true from sample to sample, although the residual resistivity ratio (abreviated RRR, and defined as $\frac{\rho(300K)}{\rho_0}$, where ρ_0 is the extrapolated resistivity for T = 0 K) varies by crystal. Typical RRR values are 600 or more, indicative of a very high purity materal. The temperature dependence of the resistivity is linear for high temperatures and levels off to values quite close to zero (but still non-zero). No transitions have been observed in these measurements in the temperature range from 1.8 K to 400 K.

4.2 Shubnikov-de Haas Results

A representative resistivity versus magnetic field sweep at constant temperature 1.8 K is shown in Figure 4.2 below. All measurements were performed on the same crystal and for fields parallel to the crystalline c-axis.

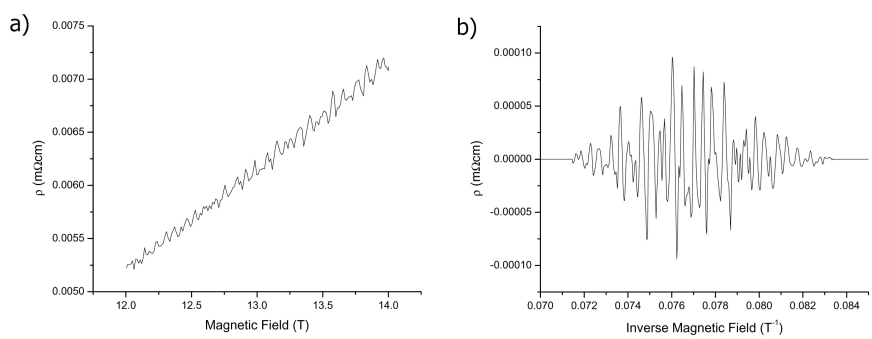

Figure 4.2: A typical resistivity versus field sweep at constant temperature. The measurement above was taken for magnetic fields between 12 T and 14 T, parallel to the c-axis, and at a temperature 1.8 K. The scanning rate was 10 Oe/s. a) The data shown is prior to a background subtraction due to a rising magnetoresistance. b) The same data as shown in a) except background subtracted and plotted versus inverse field.

The data illustrated in Figure 4.2a) is raw (i.e., no processing has yet been done). One of the most salient features depicted is a rising background due to the presence of the magnetic field. In order to account for this rising magnetoresistance, a quadratic polynomial background subtraction was employed. The 12 T to 14 T window was

chosen so as to capture many oscillations and was maintained at all measured temperatures. The sweeping rate used for all measurements was 10 Oe/s which approached the resolution limit of the PPMS.

Since theory motivates periodic behavior in inverse field (see equation (2.10)), Fourier analysis was applied to plots of background subtracted resistivity versus inverse field. A linear interpolation between points was used in order to achieve a sufficient point density for the Fourier transform algorithms. The results of this analysis are summed up in Figure 4.3.

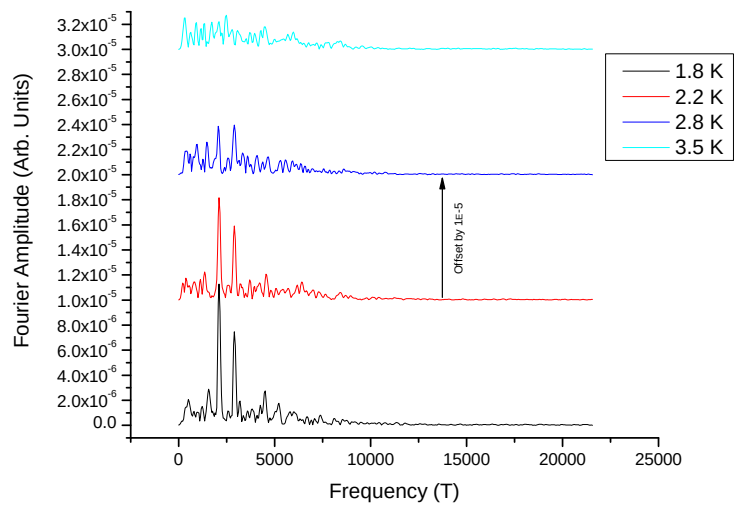

Figure 4.3: Fourier amplitude vs. frequency in Tesla. For clarity, each subsequent temperature is offset by 1×10^{-5}. By tracking the amplitude evolution as a function of temperature at specific frequency peaks, one can derive an effective mass particular to that peak. The two most prominent peaks are at 2.1 kT and 2.9 kT.

The two most prominent measured peaks are at $f_\alpha = 2.1$ kT and $f_\beta = 2.9$ kT, where we have used a Greek letter designation for each pocket for ease of reference in the later discussion. The amplitudes of the α and β peaks are significantly suppressed for increasing temperature. There is possibly a third visible peak around 4.5 kT at 1.8 K, but the signal-to-noise ratio is too low to resolve this peak for higher temperatures. The evolution of the amplitudes of the α and β peaks can be fit to the reduction factor

form given by equation (2.14) in order to estimate the effective mass of each pocket. This is done in Figure 4.4, where the assigned error bars have been estimated from the noise floor of the Fourier amplitudes depicted in Figure 4.3:

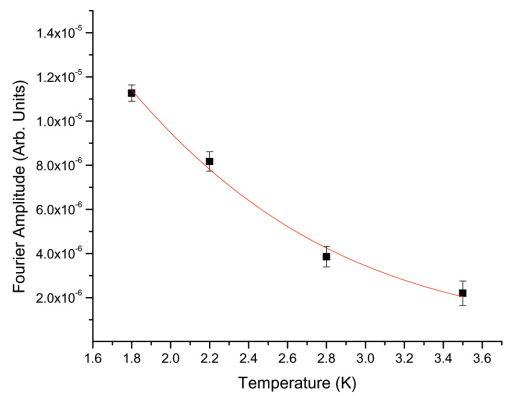

Figure 4.4: Fourier amplitude vs. temperature for the α peak. The reduction factor fit yields an estimate of the effective mass $m_\alpha = (1.3 \pm .15)m_e$.

The curve fit to the form $\frac{XT}{\sinh XT}$ shown in red in Figure 4.4 gives a parameter estimate of $X_\alpha = (1.5 \pm .17)$ K^{-1}. Since $X_\alpha = \frac{14.69m}{H}$ and $H = 13$ T (the average field over the scanned range), this gives an estimate of the effective mass for the α pocket as $m_\alpha = (1.3 \pm .15)m_e$. Doing the same analysis for the β pocket gives a parameter estimate of $X_\beta = (.69 \pm .11)$ K^{-1}, which corresponds to an effective mass $m_\beta = (.61 \pm .10)m_e$. This is represented graphically in Figure 4.5.

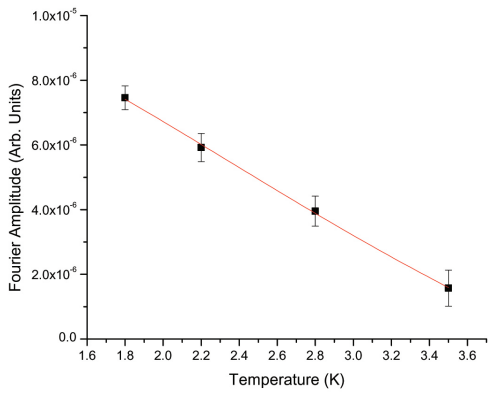

Figure 4.5: Fourier amplitude vs. temperature for the β peak. The reduction factor fit yields an estimate of the effective mass $m_\beta = (.61 \pm .10)m_e$.

4.3 Heat Capacity Results

Measured heat capacity data is plotted in Figure 4.6. In the figure, a background subtraction has been performed due to the grease and platform, which both contribute non-negligible amounts to the measured heat capacity. At each temperature, three heat capacity measurements have been performed. The error bars quoted have been computed from the standard deviation of the three measurements from the mean, uncertainties due to fitting exponentials in the two-τ scheme, and also propagation of errors due to the uncertainty in the total crystal mass.

As discussed in the introduction, the low temperature dependence of the heat capacity is given by a superposition of the phononic and electronic contributions

$$\frac{C}{T} = \gamma + AT^2, \tag{4.1}$$

where γ is the Sommerfeld coefficient, which is directly proportional to the density of states at the Fermi level. By fitting this form to the data, a value of $\gamma = 13.1 \pm .04$ mJ/mol K^2 is obtained. This value can then be directly compared with band structure calculations to determine whether or not strongly correlated electron effects are playing a major role in the dynamics of the system.

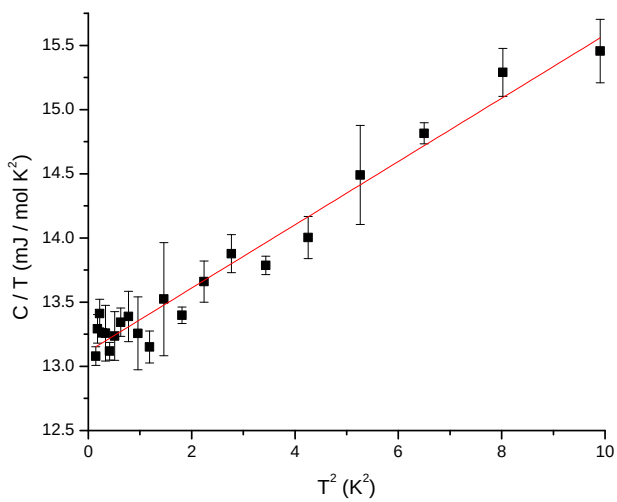

Figure 4.6: $\frac{C}{T}$ vs. T^2. By fitting a line to the data (as per the analysis in the introduction), an intercept of $\gamma = 13.1 \pm .04$ mJ/mol K^2 is extracted. This value is directly proportional to the density of states at the Fermi level.

Chapter 5

Discussion

5.1 Electronic Band Structure Calculations for $RbCu_4S_3$

The WIEN2k software package was used in order to perform theoretical Fermi surface calculations. This package employs a linearized augmented plane wave (LAPW) method in order to self-consistently solve the Kohn-Sham equations, which are obtained by variationally minimizing the total energy. Only nuclear-nuclear repulsion, electron-electron repulsion, nuclear-electron attraction, and exchange-correlation potentials are considered, and the local spin density approximation (LSDA) is used in order to choose a particular form of the exchange potential. By partitioning the primitive cell into atomic spheres and an interstitial region and using suitable boundary conditions, solutions can be expanded in terms of spherical harmonics (spherical region) and augmented plane waves (interstitial region). Many-body effects are neglected in this treatment.

The calculated Fermi surface consists of an inner 3D pocket surrounded by two larger 2D bands, as shown in Figure 5.1.

Since both 2D surfaces consist of pairs of parallel edges, $RbCu_4S_3$ might be thought to have the capability for wave vector nesting. Since all three calculated pockets are hole-like, this nesting would have to be across individual sheets. The contributions

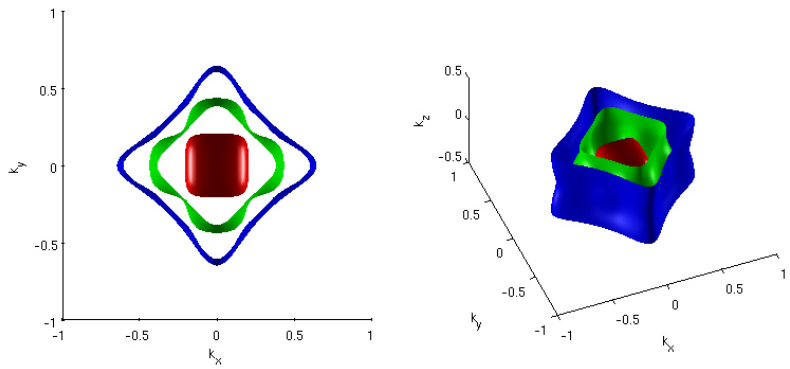

Figure 5.1: Calculated Fermi surface of $RbCu_4S_3$. The inner pocket is essentially three-dimensional, while the outer ones are two-dimensional.

of these three pockets to the density of states is summed up in the following table:

Fermi Surface Contributions to Density of States		
Pocket	Density of States (states / unit cell / eV / spin)	Sommerfeld Coefficient (mJ / mol K^2)
3D Pocket	0.233	1.099
2D Pocket (Inner)	0.667	3.145
2D Pocket (Outer)	0.823	3.880
Total	1.723	8.124

The density of states output from the WIEN2k software is converted into a Sommerfeld coefficient by use of equation (2.26) and the volume of the primitive cell.

The WIEN2k software can also compute the angle dependence of the oscillation frequencies and effective masses, as shown in Figures 5.2 and 5.3.

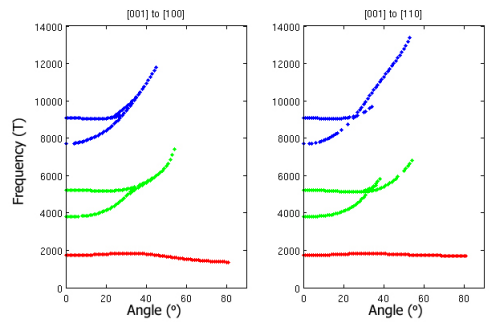

Figure 5.2: Frequencies of extremal orbits of the Fermi surface shown in Figure 5.1. The angle is measured with respect to the crystalline c-axis. The colors in the figure correspond to the bands depicted in Figure 5.1. For comparison, our preliminary experiments were performed for $\theta = 0°$.

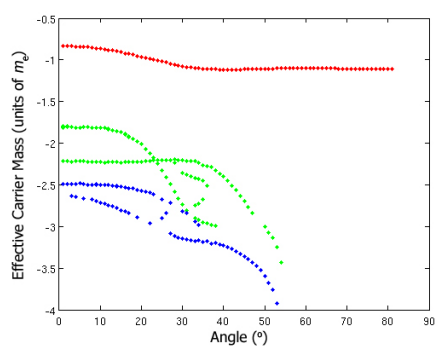

Figure 5.3: Calculated effective mass dependence against relative angle with the applied magnetic field. The measurements presented in this thesis correspond to $\theta = 0°$. Plots for two different high symmetry directions are shown. The colors correspond to the bands depicted in Figure 5.1.

5.2 Comparison with Results

Comparison of experimental frequencies with results of the band structure calculations permits a tentative assignment of orbits.

The primary detected frequency $f_\alpha = 2.1$ kT roughly corresponds to the lowest computed frequency shown in Figure 5.2; however, the extracted effective mass $m_\alpha = (1.3 \pm .15)m_e$ is higher than the theoretical prediction of $\sim .8m_e$. This discrepancy in the effective mass is most likely due to some strongly-correlated electron effects that are neglected in the WIEN2k calculations. To firmly establish this correspondence, an angle dependence measurement of the quantum oscillations is required.

It should be noted that the mass renormalization on the α peak is consistent with the discrepancy between the measured and calculated Sommerfeld coefficient. Our experimental value of $\gamma = 13.1 \pm .04$ mJ/mol K^2 exceeds the calculated value by the same factor ~ 1.6 as the effective mass ratio. Further, since $\gamma_{experimental} > \gamma_{calculated}$, apparently no significant amount of Fermi surface has been lost. This is all consistent with a very high quality metal.

The secondary detected frequency $f_\beta = 2.9$ kT with estimated effective mass $m_\beta = (.61 \pm .10)m_e$ does not correspond well to the calculations in either frequency (~ 3.9 kT) or effective mass ($\sim 2m_e$). The Fourier peak clearly indicates a frequency that is systematically smaller than the computed band structure. The discrepancy might reflect subtle differences in the energy of the calculated bands; however, further angle dependence measurements will be crucial to definitively conclude whether this is the case. Measurements to even higher fields will probably be necessary to observe evidence for the 8 kT pocket.

Chapter 6

Conclusion

Despite our initial hypothesis that the $RbCu_4S_3$ system might be a candidate for electronic instabilities due to its low-dimensional, layered structure, its formal mixed valence, and its shiny, black surface, the results here indicate that it is instead better thought of as a very high quality metal without any electronic instabilities. Via SdH analysis, two Fermi surface pockets at $\sim$ 2.1 kT and $\sim$ 2.9 kT are identified, with associated effective masses of $(1.3 \pm .15)m_e$ and $(.61 \pm .10)m_e$, respectively. One of these seemingly corresponds well to theory, although further angle dependence measurements are necessary for conclusively determining this correspondence. Through heat capacity measurements, a Sommerfeld coefficient of $\gamma = 13.1 \pm .04$ mJ/mol K^2 is extracted, which exceeds the theoretical prediction by a factor of $\sim$ 1.6. This is consistent with an effective mass renormalization.

Outstanding questions still remain about the angle dependence of the frequencies of the extremal orbits and the ability to dope away from the metallic ground state. Future work will probably broach both of these topics, in the hopes of revealing some more interesting electronic behavior and determining the nature of the detected Fermi surface pockets.

Bibliography

[1] "Spin Density Wave Anomaly at 140 K in the Ternary Iron Arsenide $BaFe_2As_2$", M. Rotter, M. Tegel, D. Johrendt, I. Schellenberg, W. Hermes, and R. Pöttgen. Phys. Rev. B **78**, 020503(R) 2008.

[2] *Density Waves in Solids*, G. Gruner, Perseus Publishing, Cambridge, 1994.

[3] *Charge Density Wave Formation in Rare-Earth Tritellurides*, N. Ru, Dissertation, Stanford University, 2008.

[4] "Neutron Scattering Study of the Interplay Between Structure and Magnetism in $Ba(Fe_{1-x}Co_x)_2As_2$, C. Lester, J. Chu, J. Analytis, S. C. Capelli, A. Erickson, C. Condron, M. Toney, I. Fisher, and S. Hayden. Phys. Rev. B **79**, 144523 2009.

[5] "Pressure-Induced Superconducting Phase in the Charge-Density-Wave Compound Terbium Tritelluride", J. Hamlin, D. Zocco, T. Sayles, and M. Maple. *Physical Review Letters*, **102**, 177002 2009.

[6] J. Folmer and F. Jellinek, *J. Less-Common Met.*, **1980**, *76*, 153.

[7] J. Tedenac, G. Brun, and M. Maurin, *Rev. Chim. Miner.*, **1981**, *18*, 69.

[8] D. Brown, J. Zubieta, P. Vella, J. Wrobleski, T. Watt, W. Hatfield, and P. Day, *Inorg. Chem.*, **1980**, *19*, 1945.

[9] K. Klepp, H. Boller, and H. Völlenkle, *Monatsh. Chem.*, **1980**, *111*, 727.

[10] B. Ghosh, M. Chaudhury, and K. Nag, *J. Solid State Chem.*, **1983**, *47*, 307.

[11] N. Hartig, P. Dorhout, and S. Miller, *J. Solid State Chem.*, **1994**, *113*, 88.

[12] "Strukturuntersuchungen an Alkalithiocupraten", W. Rudorff, H. G. Schwarz, and M. Walter, Z. Anorg. Allg. Chemie **269**, 141 (1952).

[13] "Mixed Valence Chemistry", M. Robin and P. Day, *Advances in Inorganic Chemistry and Radiochemistry*, Volume 10 (1967).

[14] *Magnetic Oscillations in Metals*, D. Schoenberg, Cambridge University Press, Cambridge, 1984.

[15] *Solid State Physics*, N. Ashcroft and N. Mermin, Thomas Learning, Inc., 1976.

[16] *Introduction to Solid State Physics: Eighth Edition*, C. Kittel, John Wiley & Sons, Inc., New York, 1996.